CHEMISTRY OF MATERIALS

pubs.acs.org/cm Article

Computationally Guided Discovery of Axis-Dependent Conduction Polarity in NaSnAs Crystals

Andrew M. Ochs, Prashun Gorai, Yaxian Wang, Michael R. Scudder, Karl Koster, Curtis E. Moore, Vladan Stevanovic, Joseph P. Heremans, Wolfgang Windl, Eric S. Toberer, and Joshua E. Goldberger*

Cite This: *Chem. Mater.* 2021, 33, 946–951 Read Online

ACCESS | Metrics & More | Article Recommendations | Supporting Information

ABSTRACT: Most electronic materials exhibit a single dominant charge carrier type, either holes or electrons, along all crystallographic directions. However, there are a small number of compounds, mostly metals, that exhibit simultaneous p-type and n-type conduction behavior along different crystallographic directions. We demonstrate that the experimental discovery of semiconductors with this axis-dependent conduction polarity can be facilitated by identifying a large anisotropy of either the electron or hole effective masses (m^*) or both, providing the electron and hole masses dominate along different crystallographic directions. We calculated the layered semiconductor NaSnAs to have a lower electron m^* in-plane than the cross-plane and a very large hole m^* in-plane and small hole m^* cross-plane. We established the growth of >3 mm-sized NaSnAs crystals via Sn flux and confirmed the band gap to be 0.65 eV, in agreement with theory. NaSnAs exhibits p-type thermopowers cross-plane and n-type thermopowers in-plane, confirming that the large anisotropy in the effective mass at the band edges is an excellent indicator for axis-dependent conduction polarity. Overall, this work shows that the discovery of semiconductors with such a phenomenon can be accelerated by computationally evaluating the anisotropic curvatures of the band edges, paving the way for their future discovery and application.

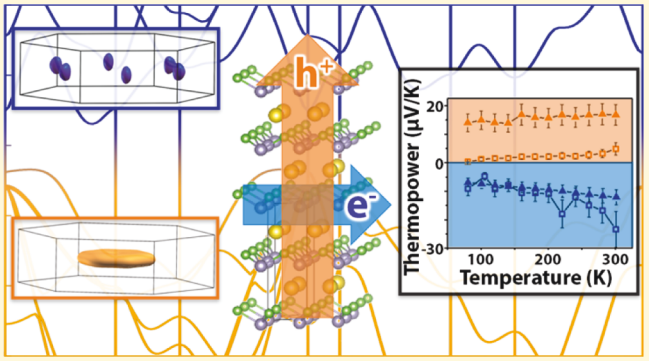

INTRODUCTION

The search for materials that simultaneously exhibit p-type and n-type conduction along different crystallographic axes has sparked considerable recent interest.[1−4] Since almost all modern electronic, optoelectronic, and thermoelectric devices require the integration of p-type and n-type semiconductors together to induce functionality, the discovery of semiconductors that have axis-dependent conduction polarity would open up the exploration of unique technologies that exploit this anisotropy in an undoped, single crystal. Of the >165,000 experimental compounds listed in the international crystal structure database, only 11 have been identified experimentally to simultaneously exhibit n-type and p-type conduction behavior along orthogonal crystallographic directions. Of these few, the only materials with semiconducting behavior are Re_4Si_7,[5] which has a 0.15 eV indirect gap,[6−8] and $CsBi_4Te_6$, which has a narrow band gap of ~0.10 eV,[9] along with the Mott insulator κ-$(BEDT\text{-}TTF)_2Cu[N(CN)_2]Cl$.[10] Due to the limited number of materials that possess this effect and the wide range of potential applications, there remains a strong need to expand the library of semiconductors that demonstrate this effect, especially to those with larger band gaps for optoelectronics.

Thus far, the overwhelming majority of materials that exhibit axis-dependent conduction polarity have been discovered serendipitously. Recently, theory has played a central role in elucidating the two known mechanisms and band structure fingerprints for axis-dependent conduction polarity and thus has the potential to facilitate the discovery of new materials.[11] In the single-carrier mechanism, a single band has opposite signs of curvatures at the Fermi level and thus effective masses (m^*) along different directions of the crystal, enabling the same carriers to behave either as electrons or holes depending on the direction of travel. In the multicarrier mechanism, the carriers that give rise to p-type conduction and n-type conduction are in different bands, such that either the valence or conduction band dominates transport along one direction, while the other band dominates transport along a different direction. In such a material, the valence or conduction band must have a small m^* along one crystallographic direction, while the other band either has a small m^* along an orthogonal direction or is relatively isotropic. A nominally undoped semiconductor could exhibit

Received: October 14, 2020
Revised: December 29, 2020
Published: January 15, 2021

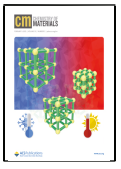

https://dx.doi.org/10.1021/acs.chemmater.0c04030
Chem. Mater. 2021, 33, 946–951

axis-dependent conduction polarity only via the multicarrier mechanism, whereas upon degenerate doping, the single-carrier mechanism could be accessed.[11] The realization of this effect via both mechanisms can be computationally predicted by calculating the anisotropic m^* values near the band edges.

Layered materials are great candidates to realize axis-dependent conduction polarity since the in-plane and cross-plane bonding directions are often composed of different orbital symmetries. Indeed, many compounds having crystal structures consisting of honeycomb networks of transition metals and/or main group atoms, which are separated by highly electropositive elements, have been predicted or found to exhibit this effect. For example, this phenomenon has recently been predicted in BaCuAs and at least 20 different isoelectronic compounds.[11] Furthermore, the layered metal $NaSn_2As_2$ was discovered to have axis-dependent conduction polarity via the single carrier mechanism.[1,12] In contrast to this "1-2-2" phase, there are a plethora of semiconducting layered Zintl phases that have a "1-1-1" stoichiometry including NaSnP, NaSnAs, and KSnSb. Through constructing a materials genome database of potential thermoelectric materials in TEDesignLab,[13,14] we have found that NaSnP and NaSnAs exhibit a unique anisotropy in the valence and conduction band m^* tensors, indicating that the hole conduction dominates transport along the cross-plane direction, while electron conduction is relatively isotropic along both directions. However, only NaSnP single crystals have been previously reported and synthesized,[15] and unfortunately, their extreme air sensitivity makes it challenging to reliably characterize their full axis-dependent transport properties. NaSnAs was discovered in 2017 and has been characterized in the bulk powder form.[16] Therefore, we set out to grow single crystals and fully evaluate the axis-dependent electrical conductivities and thermopowers of NaSnAs.

Here, we establish that NaSnAs is a semiconducting material that exhibits axis-dependent conduction polarity. The anisotropic curvatures of the valence and conduction bands lead to dominant hole conduction along the cross-plane direction and electron conduction in-plane. We developed the growth of mm-scale NaSnAs crystals via Sn flux and confirm this anisotropic conduction behavior via in-plane and cross-plane thermopower measurements. This work demonstrates how computational predictions can enable the discovery of materials that possess this conduction anisotropy.

EXPERIMENTAL METHODS

NaSnAs single crystals were synthesized and grown by a Sn flux method. Due to the air sensitivity of the starting materials and crystals, as well as the toxicity and volatility of As, the synthesis, characterization, and handling of the NaSnAs crystals discussed in this section were performed in an N_2-filled glovebox or air-free environment, unless noted otherwise. Stoichiometric amounts of Na chunks (99.9%, Aldrich), As powder (99%, STREM), and Sn powder (99.85%, Alfa Aesar) were added to a quartz tube, and additional Sn powder was added at a 12:1 mass ratio to act as a flux to facilitate crystal growth. Finally, before sealing in a larger quartz ampoule at ∼65 mTorr, quartz wool plugs were inserted into the tube above the powder to act as a filter for molten Sn. The reaction mixture was then heated to 650 °C and held for 3 h and then cooled to 400 °C at a rate of 1.5 °C/h. At 400 °C, the tubes were quenched, inverted, and rotated in a centrifuge at 1000 rpm for 10 min to separate molten Sn from the NaSnAs crystals. To further remove Sn, the NaSnAs crystals were resealed in a quartz tube and rested on top of quartz wool. Approximately, 15 single crystals from the same synthesis were then heated to 300 °C and held for 12 h to anneal the crystals and allow any excess Sn to pass through the quartz wool with additional centrifugation. This process was repeated at least three times. Sn content of single crystals was monitored after each melting procedure by removing and grinding two to three crystals each time for powder X-ray diffraction (XRD). This process was repeated until a decrease in Sn content was no longer observed. For comparison to single crystals, polycrystalline ingots of NaSnAs were prepared by grinding single crystals, pressing, and sintering in an evacuated quartz ampoule at 300 °C. Inductively coupled plasma-optical emission spectroscopy (ICP-OES) (Galbraith Laboratories) was carried out on ground single crystals to confirm the Na/Sn/As/Si using the standard protocols (GLI ME-70) and run in duplicate.

Powder XRD patterns were collected on NaSnAs with a Bruker D8 powder diffractometer with Cu Kα radiation from 2θ values from 10 to 80°. To prevent oxidation, diffraction data were collected while covering the sample with Kapton tape. The single-crystal XRD studies were carried out on a Nonius Kappa diffractometer equipped with a Bruker APEX-II CCD and Mo K_α radiation (λ = 0.71073 Å). A 0.570 × 0.446 × 0.272 mm piece of a metallic silver block was mounted on a Cryoloop with clear enamel. Data were collected in a nitrogen gas stream at 300(2) K using ϕ and ϖ scans. The crystal-to-detector distance was 40 mm, and the exposure time was 10 s per frame using a scan width of 2.0°. Data collection was 100% complete to 25.00° in θ. A total of 3595 reflections were collected covering the indices $-4 \le h \le 5$, $-5 \le k \le 5$, and $16 \le l \le 16$. A total of 236 reflections were found to be symmetry-independent, with an R_{int} of 0.0458. Indexing and unit cell refinement indicated a primitive, hexagonal lattice. The space group was found to be $P6_3mc$. The data were integrated using the Bruker SAINT software program and scaled using the SADABS software program. Solution by direct methods (SHELXT) produced a complete phasing model for refinement. All atoms were refined anisotropically by full-matrix least-squares (SHELXL-2014).

Kubelka−Munk (K−M) diffuse reflectance infrared Fourier transform spectroscopy (DRIFTS) measurements were performed in the infrared region using a PerkinElmer Frontier dual-range spectrometer with an integrating sphere in a nitrogen glovebox. The absorbance of ground NaSnAs powder dispersed in dried KBr (Sigma-Aldrich) from 0.05 to 0.99 eV was collected, following collection of a KBr background spectrum. Additionally, diffuse reflectance absorbance (DRA) data were collected for the visible range (>0.75 eV) using a PerkinElmer Lambda 950 UV/vis spectrophotometer fitted with an integrating sphere using an air-free sample holder. The samples were diluted and dispersed in $BaSO_4$ (Sigma-Aldrich) and measured using an air-free sample holder with a quartz window.

Thermoelectric transport properties were measured using a standard liquid N_2 cryostat at temperatures ranging from 80 to 300 K. A small brass sheet was attached to the top of the crystal underneath a resistance heater, and an alumina sheet acted as a heat sink, assuring uniform heat flow in the samples. Copper−constantan thermocouples were attached at two points along the crystal with Ag epoxy to measure the temperature gradient, and the copper legs of the thermocouples were also used to measure the Seebeck voltage. Thermal conductivity measurements were collected along the in-plane direction using the classical heater-and-sink method, where the amount of heater power divided by the temperature drop across the sample gives the thermal conductance, which is converted to conductivity, given the dimensions. Current wires were added to the crystal for the collection of resistivity measurements. For Hall coefficient measurements along the in-plane direction, an additional set of copper wires were attached in a direction transverse to both heat flow and the applied magnetic field, which was varied from −1.4 T to +1.4 T. Thermopower and resistivity measurements were first performed in the in-plane orientation, and then, contacts were removed and reattached in the cross-plane orientation, allowing for measurements in both directions to be collected on the same single crystal.

The electronic properties of NaSnAs were calculated using density functional theory (DFT) as implemented in the Vienna Abinitio Simulation Package (VASP)[17,18] with projector augmented wave Perdew−Burke−Ernzerhof (PAW-PBE) potentials.[19] The kinetic energy cutoff for plane waves was set to 360 eV for relaxations and electronic structure, and the Brillouin-zone integration was performed on a Γ-centered 12 × 12×3 k-point mesh. For the electronic structure

https://dx.doi.org/10.1021/acs.chemmater.0c04030
Chem. Mater. 2021, 33, 946−951

calculations, an HSE hybrid-functional[20] calculation was performed. The fraction of exact exchange was set to 10% and the range−separation parameter was set to 0.2, which results in a band gap whose value matches the experimental measurements for relaxed lattice constants of a = 4.03 Å and c = 12.12 Å.

RESULTS AND DISCUSSION

The crystal structure of NaSnAs is composed of puckered, honeycomb SnAs sheets separated by Na atoms (Figure 1a).

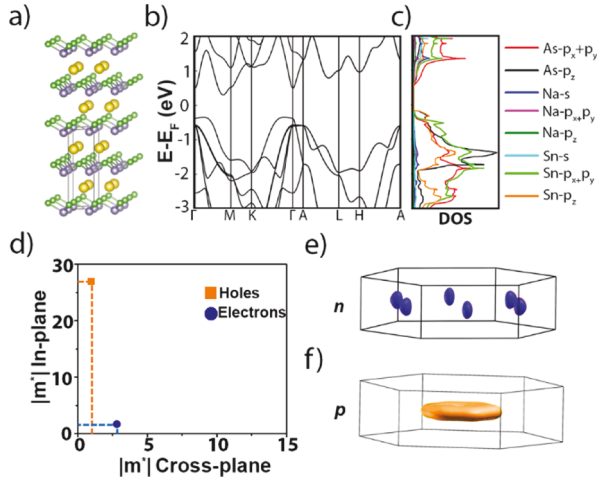

Figure 1. (a) Crystal structure of NaSnAs. Yellow atoms represent Na, silver atoms represent Sn, and green atoms represent As. (b) Band structure and partial density of states (PDOS) of NaSnAs. (d) Anisotropic, in-plane, and cross-plane effective masses for holes and electrons in NaSnAs. (e) Fermi surface of the conduction band 0.06 eV above the CBM. (f) Fermi surface of the valence band 0.04 eV below the VBM.

Within each layer, the Sn and As atoms alternate positions to form a hexagonal BN-like arrangement. There exist two SnAs layers per unit cell such that the Sn atoms in one layer are directly above the Sn atoms in the next layer; however, the As layers alternate positions, leading to a $P6_3mc$ space group. Considering the large electropositive nature of Na, one can consider the SnAs covalent layers to be reduced to $[SnAs]^-$, with the Na atom oxidized to Na^+. Assuming that this electron is donated to the Sn atoms, both As and Sn would feature formal octets with three covalent bonds and one lone pair. The lone pair on Sn or As is positioned either above or below the layers, leading to the observed puckering in the unit cell. This assignment of Na^+ and $[SnAs]^-$ is in excellent agreement with calculations of the Bader charges based on the crystal structure (Table S1).

The electronic structure and the partial density of states (PDOS) of NaSnAs were calculated using DFT within the hybrid-functional approach (Figure 1b,c). This material is predicted to be a 0.64 eV indirect gap semiconductor. The valence band maximum is slightly shifted away from Γ, between Γ and K/M. At Γ, the highest energy valence band is predominantly composed of filled Sn 5p$_z$ and As 4p$_z$ orbitals in a π^* configuration (Figure S1a). Since the p$_z$ orbitals have very little orbital overlap within each puckered SnAs sheet, the valence band has minimal dispersion in energy along the in-plane directions (Γ to M or Γ to K). Since most of the electron density of the p$_z$ orbitals occurs along the cross-plane direction, the valence band has a much larger dispersion from Γ to Z. The conduction band minimum occurs as a low energy pocket between Γ and M, close to M. The conduction band minimum is mainly σ^* character between the Sn−As p$_x$ and p$_y$ orbitals along the in-plane direction including contribution from the Na 3s orbitals (Figure S1b). Therefore, the conduction band minimum has large dispersion along both the in-plane and cross-plane directions.

To fully evaluate the anisotropy in the conduction and valence bands, we calculated the effective mass tensors of the conduction and valence band edges for NaSnAs. To understand and compare the magnitude in anisotropy of NaSnAs to similar isoelectronic compounds, we also calculated the effective mass tensors of semiconducting phases KSnAs and KSnSb (Table S2, Figure S2). For NaSnAs, the hole effective masses were calculated as |27 m_0| and |0.96 m_0| (|0.65 m_0| and |0.12 m_0| for KSnSb, m_0 = free electron mass) for the in-plane and cross-plane directions, respectively. The calculated electron effective masses for NaSnAs are 1.7 m_0 and 2.8 m_0 (0.35 m_0 and 0.17 m_0 for KnSnSb) for the in-plane and cross-plane directions, respectively. The plotted effective masses, in Figure 1d, illustrate the large anisotropy in NaSnAs that leads to axis-dependent conduction. In addition, the calculated Fermi surfaces of the hole and electron pockets further exemplify the large anisotropy of the band curvature that leads to axis-dependent conduction polarity.[11] The Fermi surface 0.06 eV above the CBM consists of six prolate ellipsoids (Figure 1e), while the Fermi surface 0.04 eV below the VBM has an extremely oblate-shaped ellipsoid (Figure 1f). Given that carrier mobility is strongly dependent on the effective mass integrated over all bands, the prediction of holes to have much larger |m^*| in-plane and electrons to have larger m^* cross-plane indicates that this material will have a unique intrinsic conduction anisotropy with both carriers present.

To verify the existence of axis-dependent conduction polarity, single crystals of NaSnAs >3 mm in length and width were grown using a Sn flux method (Figure 2a). The NaSnAs crystal

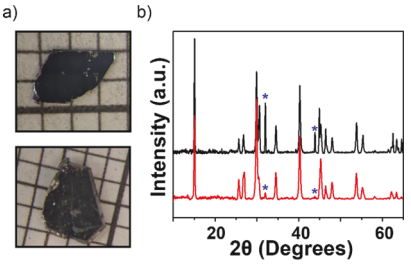

Figure 2. (a) Photographs of NaSnAs single crystals grown from Sn flux. Gridlines represent 1 mm. (b) Powder XRD patterns before (black) and after (red) Sn-removal procedure. Blue asterisks indicate location of major Sn impurity peaks that have no overlap with NaSnAs reflections.

structure was obtained and confirmed using single crystal diffraction measurement and included in the Supporting Information. After growth, residual Sn is observed in the XRD pattern of ground-up crystals. In other reports of crystal growth in Sn flux, excess Sn is commonly removed with dilute HCl.[21] However, since NaSnAs is not stable in HCl, excess flux was removed by repeated melting and centrifugation of the crystals with residual Sn present. The powder XRD patterns, in Figure 2b, confirm the removal of a large fraction of Sn through this process. Rietveld analysis before and after purification (Figures S3 and S4; Tables S3 and S4) displays a phase fraction decrease from 15.4% to 1.8% residual Sn impurity. In addition, ICP-OES analysis confirms the 1:1:1 atomic ratio of Na/Sn/As (Table S5)

https://dx.doi.org/10.1021/acs.chemmater.0c04030
Chem. Mater. 2021, 33, 946−951

and minimal (~16.3 ppm) Si contamination from the quartz tube.

DRA measurements were performed on NaSnAs powder (Figure 3) in the infrared and visible regions to analyze and

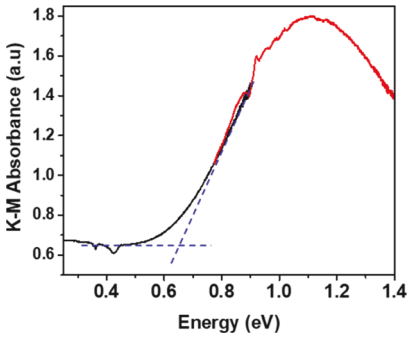

Figure 3. DRIFTS of NaSnAs powder dispersed in KCl. The observed optical transition occurs at 0.66 eV.

confirm the semiconducting nature of this material. Reflectance data were converted to absorption using the Kubelka–Munk equation, and the absorption spectrum shows a sharp optical transition at ~0.66 eV. To accurately deduce the band gap from the absorption spectrum, we modeled the absorbance spectrum following the Tauc–Davis–Mott expressions for the possible optical transitions that can occur in NaSnAs, assuming both a 3D direct allowed and 3D indirect allowed transition (Figure S5). The indirect transition was determined to be at a lower energy of 0.65 eV, while the direct transition occurs at 0.76 eV. These measurements agree with the values predicted from theory (Figure 2b), for which the indirect and direct gaps are calculated at 0.64 and 0.82 eV, respectively.

To characterize the conduction polarity of NaSnAs, the in-plane and cross-plane thermopowers on two separate crystals were measured. The thermopower values were measured from 80–300 K along the in-plane and cross-plane directions. Axis-dependent conduction polarity was confirmed on both crystals (Figure 4e). Thermopowers on both crystals exhibit negative values along the in-plane direction that become more negative with increasing temperature, reaching values of −12.1 and −23.4 μV/K for crystals 1 and 2, respectively, at 300 K. The cross-plane thermopowers are positive and increase with increasing temperature, reaching magnitudes of +16.8 and +4.8 μV/K for crystals 1 and 2, respectively.

The differences in thermopowers between the two crystals may be a result of slightly different carrier concentrations, differing amounts of residual Sn impurities between the measured crystals, and/or a difference in electron scattering times. Due to the crystals being neither strongly p- nor n-type, we do not observe a strong temperature dependence of thermopower, typical of semiconducting materials, and any difference in temperature dependence observed in the sample is likely the result of a difference in electron scattering times. In agreement with the XRD patterns, small amounts of residual Sn were observed on the outer faces and edges of the crystal based on scanning electron microscopy (SEM) and energy dispersive X-ray spectroscopy (EDX) measurements (Figure S6). Multiple crystals were cleaved in half, and EDX maps of the cross section were obtained. However, no Sn inclusions could be detected in the cross section, indicating that the majority of residual exists on the outer surface.

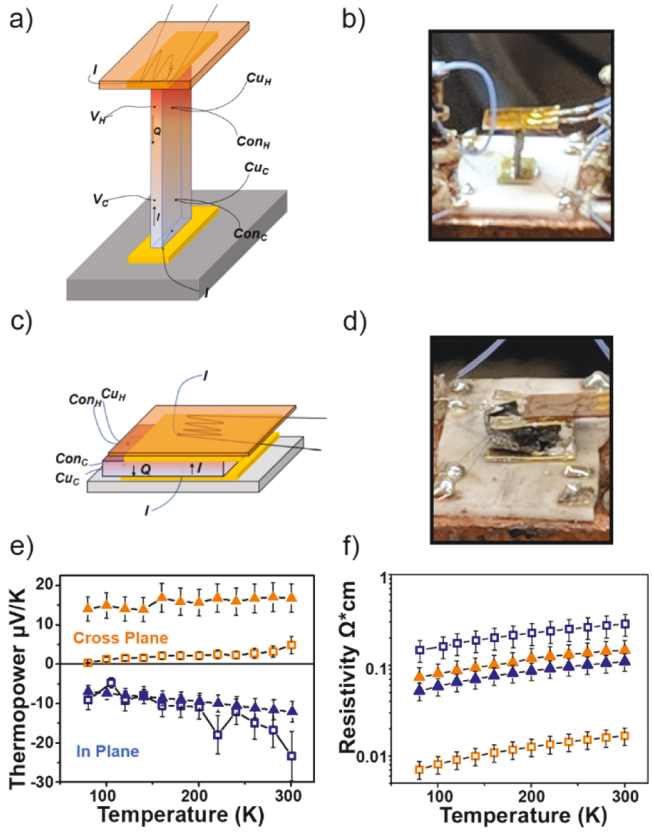

Figure 4. (a) Schematic illustrating the in-plane thermopower and resistivity measurement. (b) Photograph of in-plane measurement. (c) Schematic illustrating the cross-plane thermopower and resistivity measurement. (d) Photograph of cross-plane measurement. (e,f) In-plane and cross-plane thermopowers and electrical resistivities for crystals 1 and 2. Crystal 1 is designated by triangles, and crystal 2 is designated by squares. Cross-plane measurements are orange, and in-plane measurements are blue.

The in-plane and cross-plane resistivities both exhibit a positive slope with increasing temperature. While this behavior is typically indicative of metallic behavior, it is likely a result of the presence of extrinsic doping effects via atomic vacancies and inclusions and/or residual Sn on the surface of the crystal. Based on the Hall measurements performed along the in-plane direction on crystal 2 (Figure S7), the carrier concentration is ~4×10^{19} cm^{-3} at 300 K.

Interestingly, the in-plane resistivities for both crystals were higher than those along the cross-plane direction. While this is unusual in layered materials, we hypothesize that it is a consequence of the fact that both the electron and hole cross-plane effective masses are much smaller and close in magnitude (2.8 m_0 and |0.96|m_0, respectively), allowing conduction of both carriers. In contrast, the in-plane hole effective mass (|27|m_0) is much larger than the electron effective mass (1.7 m_0), reducing the contribution of holes along this direction. Furthermore, the temperature-dependent thermal conductivity of crystal 2 was measured along the in-plane direction as well. The thermal conductivity value decreased with increasing temperature, with a room-temperature value of 2.0 W m^{-1} K^{-1} (Figure S8). To verify the measurement results and compare with previous studies on this material, the thermal conductivity was also measured on a polycrystalline ingot, resulting in a value of 1.6 W m^{-1} K^{-1} at 300 K. The extrapolation of the data to 300 K is consistent with a previous study on polycrystalline ingots.[16]

https://dx.doi.org/10.1021/acs.chemmater.0c04030
Chem. Mater. 2021, 33, 946–951

The transport data collected on crystals 1 and 2 strike a significant contrast with the data collected on NaSnAs crystals contaminated with the 15.4% phase fraction of Sn (Figure S9). Despite the large amount of Sn impurity, this crystal still exhibits positive and negative thermopowers along the in-plane and cross-plane directions at room temperature, highlighting the robust nature of axis-dependent conduction polarity in NaSnAs, even with the large presence of a metallic impurity. This also indicates that further improvement in the crystal growth and reduction of Sn contaminants can fully unlock the large values and opposite signs of thermopower that are expected in NaSnAs.

CONCLUSIONS

We have shown that the discovery of semiconductors that exhibit axis-dependent conduction polarity can be expanded through identifying compounds that have either a highly anisotropic valence or conduction band or both, provided the directions where m^* is small are different. Based on these predictions, a Sn-flux growth of millimeter-sized single crystals of NaSnAs was developed. The in-plane and cross-plane thermopowers on multiple crystals were found to be negative and positive, respectively, confirming these predictions. Of the extremely small number of semiconductors discovered to exhibit this exotic conduction behavior, NaSnAs has the largest band gap (0.65 eV) by far and thus is an excellent material targeting the future exploration of optoelectronic applications that exploit this effect.

ASSOCIATED CONTENT

Supporting Information

The Supporting Information is available free of charge at https://pubs.acs.org/doi/10.1021/acs.chemmater.0c04030.

Calculated orbital wavefunctions of the conduction and valence bands, Bader charge analysis of NaSnAs, ICP-OES measurements, Rietveld analysis of the NaSnAs crystals before and after residual Sn removal, Tauc–Davis–Mott plots highlighting the direct and indirect transitions, SEM/EDX images that highlight residual Sn on the surface of NaSnAs crystals, temperature-dependent Hall coefficient and carrier concentration of NaSnAs crystals, in-plane temperature-dependent thermal conductivity of the NaSnAs crystal, and thermopower and resistivity measurements of the heavily Sn-contaminated crystals (PDF)

NaSnAs crystal structure (CIF)

AUTHOR INFORMATION

Corresponding Author

Joshua E. Goldberger − *Department of Chemistry and Biochemistry, The Ohio State University, Columbus, Ohio 43210, United States;* orcid.org/0000-0003-4284-604X; Email: goldberger.4@osu.edu

Authors

Andrew M. Ochs − *Department of Chemistry and Biochemistry, The Ohio State University, Columbus, Ohio 43210, United States*

Prashun Gorai − *Department of Metallurgical and Materials Engineering, Colorado School of Mines, Golden, Colorado 80401, United States;* orcid.org/0000-0001-7866-0672

Yaxian Wang − *Department of Materials Science and Engineering, The Ohio State University, Columbus, Ohio 43210, United States*

Michael R. Scudder − *Department of Chemistry and Biochemistry, The Ohio State University, Columbus, Ohio 43210, United States*

Karl Koster − *Department of Chemistry and Biochemistry, The Ohio State University, Columbus, Ohio 43210, United States*

Curtis E. Moore − *Department of Chemistry and Biochemistry, The Ohio State University, Columbus, Ohio 43210, United States;* orcid.org/0000-0002-3311-7155

Vladan Stevanovic − *Department of Metallurgical and Materials Engineering, Colorado School of Mines, Golden, Colorado 80401, United States*

Joseph P. Heremans − *Department of Mechanical and Aerospace Engineering and Department of Physics, The Ohio State University, Columbus, Ohio 43210, United States*

Wolfgang Windl − *Department of Materials Science and Engineering, The Ohio State University, Columbus, Ohio 43210, United States*

Eric S. Toberer − *Department of Physics, Colorado School of Mines, Golden, Colorado 80401, United States*

Complete contact information is available at: https://pubs.acs.org/10.1021/acs.chemmater.0c04030

Author Contributions

The manuscript was written through contributions of all authors.

Notes

The authors declare no competing financial interest.

ACKNOWLEDGMENTS

A.M.O., M.R.S., and J.E.G. acknowledge NSF EFRI-1433467 for primary support. Y.W., K.K., and W.W. acknowledge support from AFOSR project no. FA9550-18-1-0335 for funding. Computations were performed on the machines of the Ohio Supercomputer Center under project no. PAS0072. J.P.H. acknowledges support from DOE project no. DE-SC0020923. P.G., V.S., and E.S.T. acknowledge support from NSF DMR-1729594.

REFERENCES

(1) He, B.; Wang, Y.; Arguilla, M. Q.; Cultrara, N. D.; Scudder, M. R.; Goldberger, J. E.; Windl, W.; Heremans, J. P. The Fermi surface geometrical origin of axis-dependent conduction polarity in layered materials. *Nat. Mater.* **2019**, *18*, 568–572.

(2) Tang, Y.; Cui, B.; Zhou, C.; Grayson, M. p × n-Type Transverse Thermoelectrics: A Novel Type of Thermal Management Material. *J. Electron. Mater.* **2015**, *44*, 2095–2104.

(3) Zhou, C.; Birner, S.; Tang, Y.; Heinselman, K.; Grayson, M. Driving Perpendicular Heat Flow: p x n-Type Transverse Thermoelectrics for Microscale and Cryogenic Peltier Cooling. *Phys. Rev. Lett.* **2013**, *110*, 227701.

(4) Scudder, M. R.; He, B.; Wang, Y.; Rai, A.; Cahill, D. G.; Windl, W.; Heremans, J. P.; Goldberger, J. G. High transverse thermoelectric figure of merit in Re4Si7 and its electronic-structure origin, **2020**, Submitted.

(5) Harada, S.; Tanaka, K.; Kishida, K.; Inui, H. Crystal Structure and Thermoelectric Properties of $ReSi_{1.75}$ Based Alloys. *Adv. Mater. Res.* **2007**, *26–28*, 197–200.

(6) Nguyen, T.; Veuillen, J.; Muret, P.; Kennou, S.; Siokou, A. E.; Ladas, S.; Lahatra Razafindramisa, F.; Brunel, M. Semiconducting rhenium silicide thin films on Si(111). *J. Appl. Phys.* **1995**, *77*, 2514–2518.

(7) Long, R. G.; Bost, M. C.; Mahan, J. E. Optical and electrical properties of semiconducting rhenium disilicide thin films. *Thin Solid Films* **1988**, *162*, 29−40.
(8) Ali, I.; Muret, P.; Nguyen Tan, T. A. Properties of semiconducting rhenium silicide thin films grown epitaxially on silicon (111). *Appl. Surf. Sci.* **1996**, *102*, 147−150.
(9) Chung, D.-Y.; Hogan, T. P.; Rocci-Lane, M.; Brazis, P.; Ireland, J. R.; Kannewurf, C. R.; Bastea, M.; Uher, C.; Kanatzidis, M. G. A new thermoelectric material: $CsBi_4Te_6$. *J. Am. Chem. Soc.* **2004**, *126*, 6414−6428.
(10) Kawasugi, Y.; Seki, K.; Edagawa, Y.; Sato, Y.; Pu, J.; Takenobu, T.; Yunoki, S.; Yamamoto, H. M.; Kato, R. Simultaneous enhancement of conductivity and Seebeck coefficient in an organic Mott transistor. *Appl. Phys. Lett.* **2016**, *109*, 233301.
(11) Wang, Y.; Koster, K. G.; Ochs, A. M.; Scudder, M. R.; Heremans, J. P.; Windl, W.; Goldberger, J. E. The Chemical Design Principles for Axis-Dependent Conduction Polarity. *J. Am. Chem. Soc.* **2020**, *142*, 2812−2822.
(12) Wang, Y.; Narang, P. Anisotropic scattering in the goniopolar metal $NaSn_2As_2$. *Phys. Rev. B* **2020**, *102*, 125122.
(13) Gorai, P.; Gao, D.; Ortiz, B.; Miller, S.; Barnett, S.; Mason, T.; Lv, Q.; Stevanovic, V.; Toberer, E. TE Design Lab: A virtual laboratory for thermoelectric material design. *Comput. Mater. Sci.* **2015**, *112*, 368−376.
(14) Gorai, P.; Ganose, A.; Faghaninia, A.; Jain, A.; Stevanović, V. Computational discovery of promising new n-type dopable ABX Zintl thermoelectric materials. *Mater. Horiz.* **2020**, *7*, 1809.
(15) Arguilla, M. Q.; Cultrara, N. D.; Scudder, M. R.; Jiang, S.; Ross, R. D.; Goldberger, J. E. Optical Properties and Raman-Active Phonon Modes in Two-Dimensional Honeycomb Zintl Phases. *J. Mater. Chem. C* **2017**, *5*, 11259.
(16) Lin, Z.; Wang, G.; Le, C.; Zhao, H.; Liu, N.; Hu, J.; Guo, L.; Chen, X. Thermal conductivities in NaSnAs, NaSnP, and $NaSn_2As_2$: Effect of double lone-pair electrons. *Phys. Rev. B* **2017**, *95*, 165201.
(17) Kresse, G.; Hafner, J. Ab initio molecular dynamics for liquid metals. *Phys. Rev. B: Condens. Matter Mater. Phys.* **1993**, *47*, 558−561.
(18) Kresse, G.; Hafner, J. Ab initio molecular-dynamics simulation of the liquid-metal–amorphous-semiconductor transition in germanium. *Phys. Rev. B: Condens. Matter Mater. Phys.* **1994**, *49*, 14251−14269.
(19) Kresse, G.; Joubert, D. From ultrasoft pseudopotentials to the projector augmented-wave method. *Phys. Rev. B: Condens. Matter Mater. Phys.* **1999**, *59*, 1758−1775.
(20) Heyd, J.; Scuseria, G. E.; Ernzerhof, M. Hybrid functionals based on a screened Coulomb potential. *J. Chem. Phys.* **2003**, *118*, 8207−8215.
(21) Kanatzidis, M. G.; Pöttgen, R.; Jeitschko, W. The Metal Flux: A Preparative Tool for the Exploration of Intermetallic Compounds. *Angew. Chem., Int. Ed.* **2005**, *44*, 6996−7023.

https://dx.doi.org/10.1021/acs.chemmater.0c04030
Chem. Mater. 2021, 33, 946−951